Supplement of Earth Syst. Sci. Data, 18, 6421–6433, 2026
https://doi.org/10.5194/essd-18-6421-2026-supplement

Supplement of

A Global Surface Turbulence Heat Flux Dataset resolving tropical cyclones

Weixiang Peng et al.

Correspondence to: Zhanhong Ma (mazhanhong17@nudt.edu.cn)

The supplementary information primarily comprises several heat flux products (J-OFURO 3, ifremerflux, and OAFlux), which include global distribution maps, horizontal distribution under varying tropical cyclone (TC) conditions, and time evolution diagrams. Comparative analysis of these elements allows for a clearer identification and understanding of the key strengths and weaknesses of GHFD.

Figure S1–S6 depict the global distribution of sensible heat and latent heat for J-OFURO 3, ifremerflux and OAFlux on March 1st, June 1st, September 1st, and December 1st, 2007. From the comparison of the figures, it can be seen that the positions, ranges, and magnitudes of the maximum and minimum values of these heat flux products vary little among different seasons, yet all exhibit the same significant seasonal variability. The comparison with the global distribution of the GHFD product (Figure 3–4) can demonstrate the feasibility of the GHFD product under no-TCs condition.

Figure S7–S12 present the horizontal distribution of different heat flux products under varying TC intensities. These results show that heat flux in all three products increases with the TC intensity rises, which is consistent with previous theoretical studies. Notably, compared with Figure 5–6, the GHFD product exhibits a significantly stronger linear variation in surface heat flux.

Figure S13–S15 illustrate the temporal evolution of three heat flux products during the passage of the TC. In comparison to Figure 7, all heat flux products show an increase in heat flux values during the TC. Notably, the GHFD product exhibits a higher magnitude than the other products, and displays a more pronounced cold wake effect.

Figure S16 shows the bias comparison of 2 m temperature, 2 m specific humidity, and 10-m wind speed between COARE3.6 and numerical model, used to compare the discrepancy values between them.

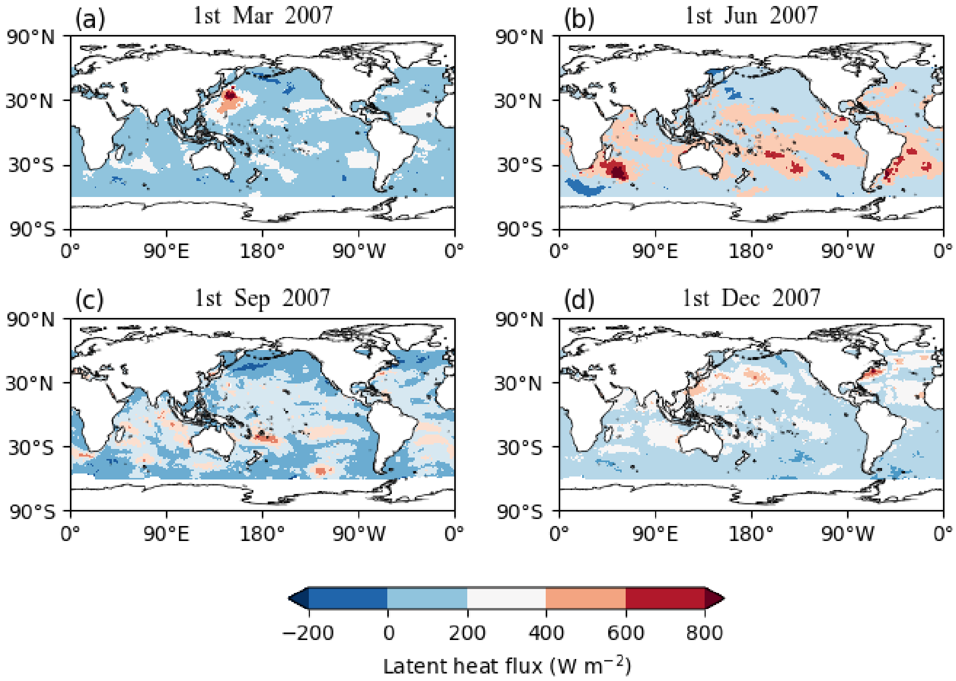

Figure S1: The global distribution of the surface latent heat flux (W m^{-2}) from 60°S to 60°N on (a) March 1, 2007, (b) June 1, 2007, (c) September 1, 2007 and (d) December 1, 2007 for J-OFURO 3.

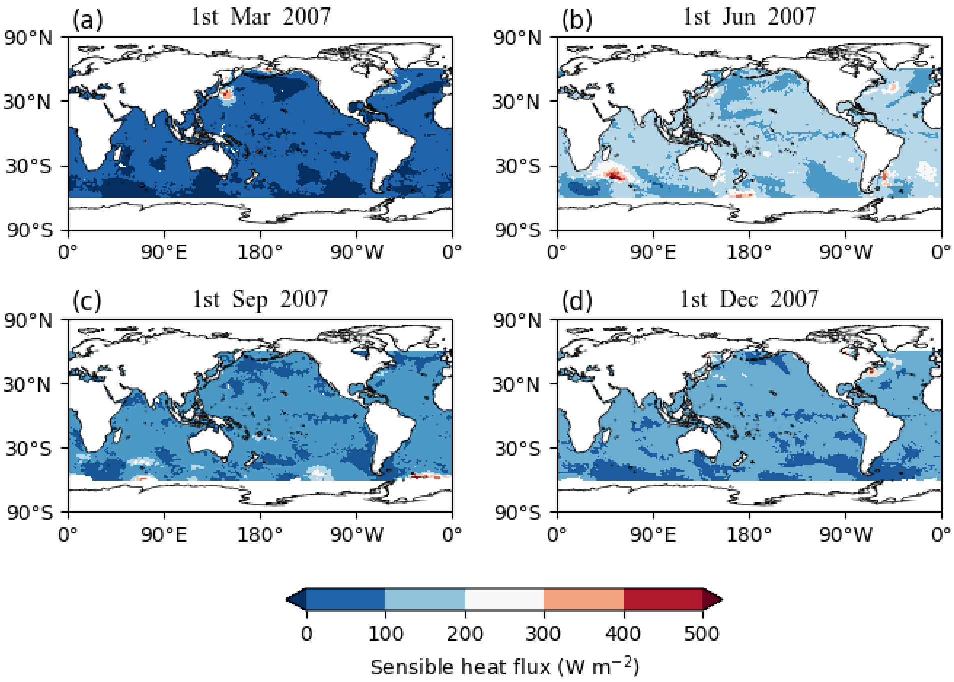

Figure S2: The global distribution of the surface sensible heat flux (W m^{-2}) from 60°S to 60°N on (a) March 1, 2007, (b) June 1, 2007, (c) September 1, 2007 and (d) December 1, 2007 for J-OFURO 3.

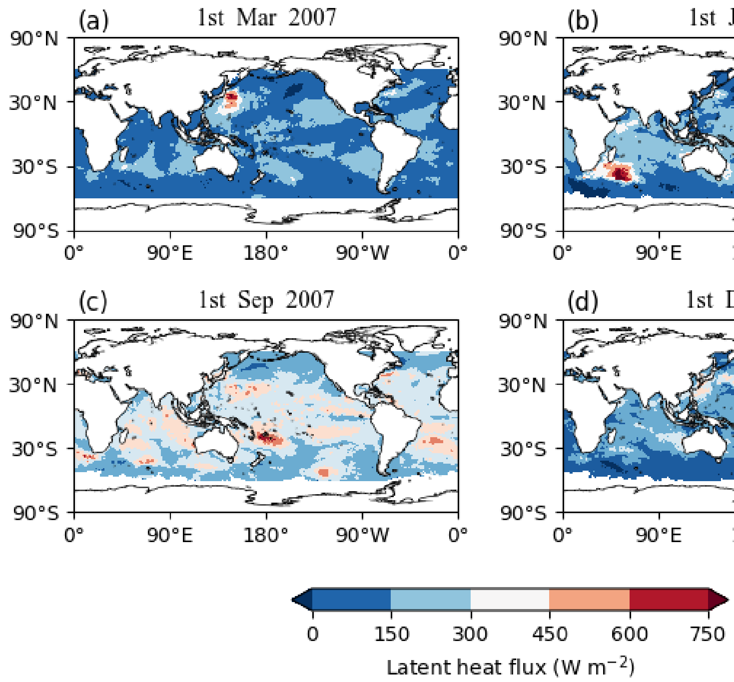

Figure S3: The global distribution of the surface latent heat flux (W m^{-2}) from 60°S to 60°N on (a) March 1, 2007, (b) June 1, 2007, (c) September 1, 2007 and (d) December 1, 2007 for ifremerflux.

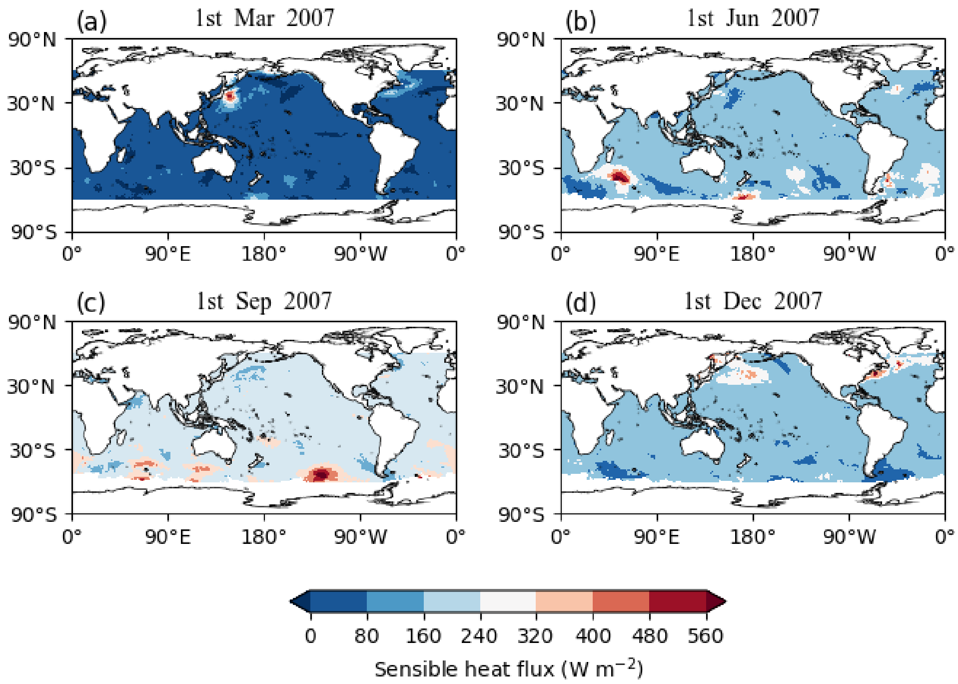

Figure S4: The global distribution of the surface sensible heat flux (W m^{-2}) from 60°S to 60°N on (a) March 1, 2007, (b) June 1, 2007, (c) September 1, 2007 and (d) December 1, 2007 for ifremerflux.

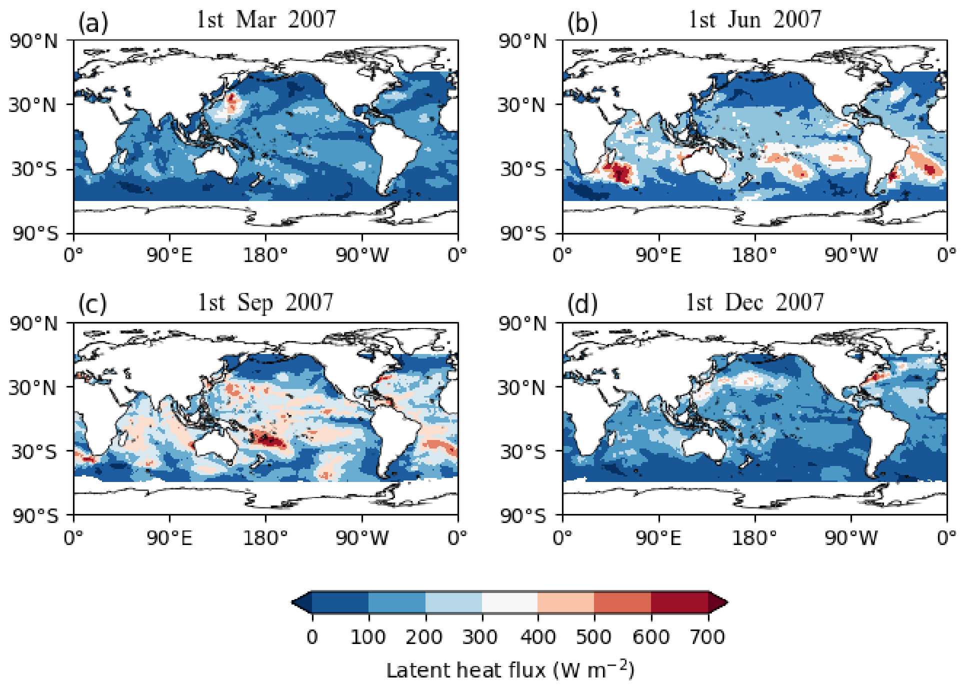

Figure S5: The global distribution of the surface latent heat flux (W m^{-2}) from 60°S to 60°N on (a) March 1, 2007, (b) June 1, 2007, (c) September 1, 2007 and (d) December 1, 2007 for OAFlux.

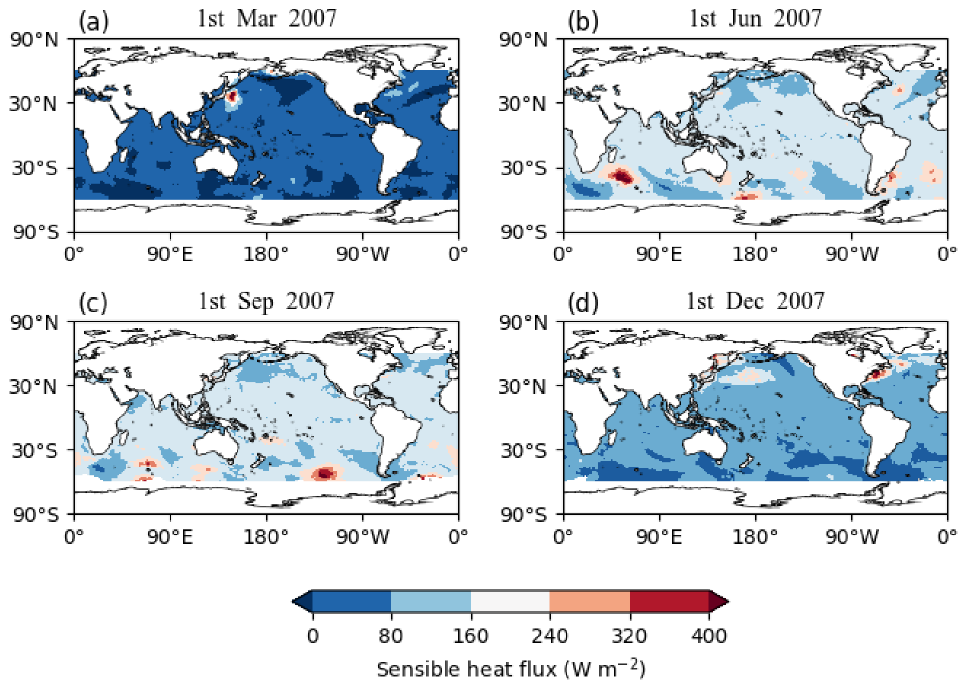

Figure S6: The global distribution of the surface sensible heat flux (W m^{-2}) from 60°S to 60°N on (a) March 1, 2007, (b) June 1, 2007, (c) September 1, 2007 and (d) December 1, 2007 for OAFlux.

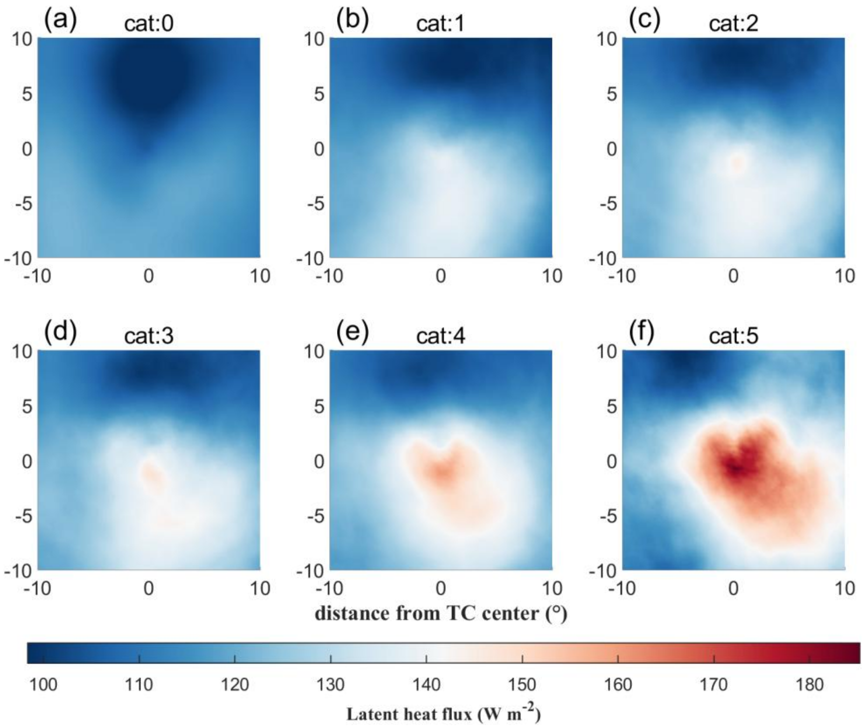

Figure S7: Plan views of composite surface latent heat flux (W m^{-2}) centered on TC classified by TC intensity with (a) Cat 0, (b) Cat 1, (c) Cat 2, (d) Cat 3, (e) Cat 4, and (f) Cat 5 for J-OFURO 3.

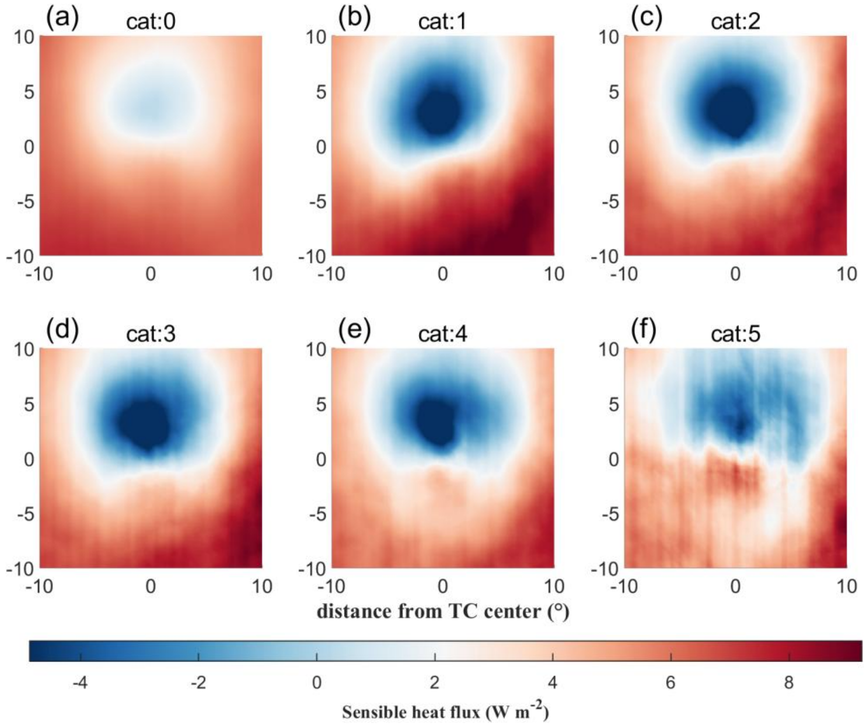

Figure S8: Plan views of composite surface sensible heat flux (W m^{-2}) centered on TC classified by TC intensity with (a) Cat 0, (b) Cat 1, (c) Cat 2, (d) Cat 3, (e) Cat 4, and (f) Cat 5 for J-OFURO 3.

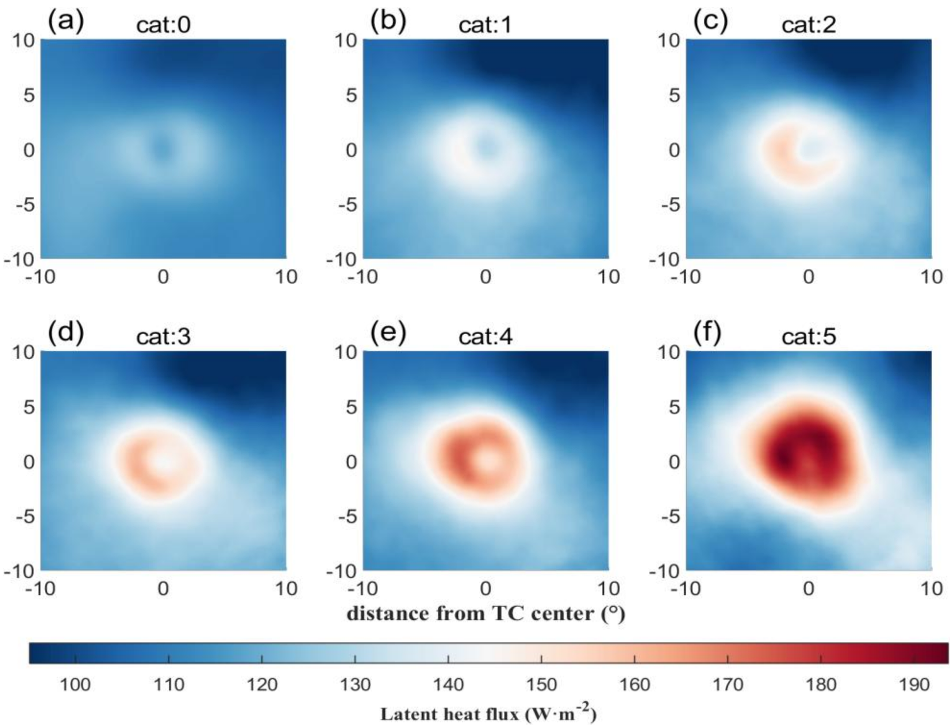

Figure S9: Plan views of composite surface latent heat flux (W m^{-2}) centered on TC classified by TC intensity with (a) Cat 0, (b) Cat 1, (c) Cat 2, (d) Cat 3, (e) Cat 4, and (f) Cat 5 for ifremerflux.

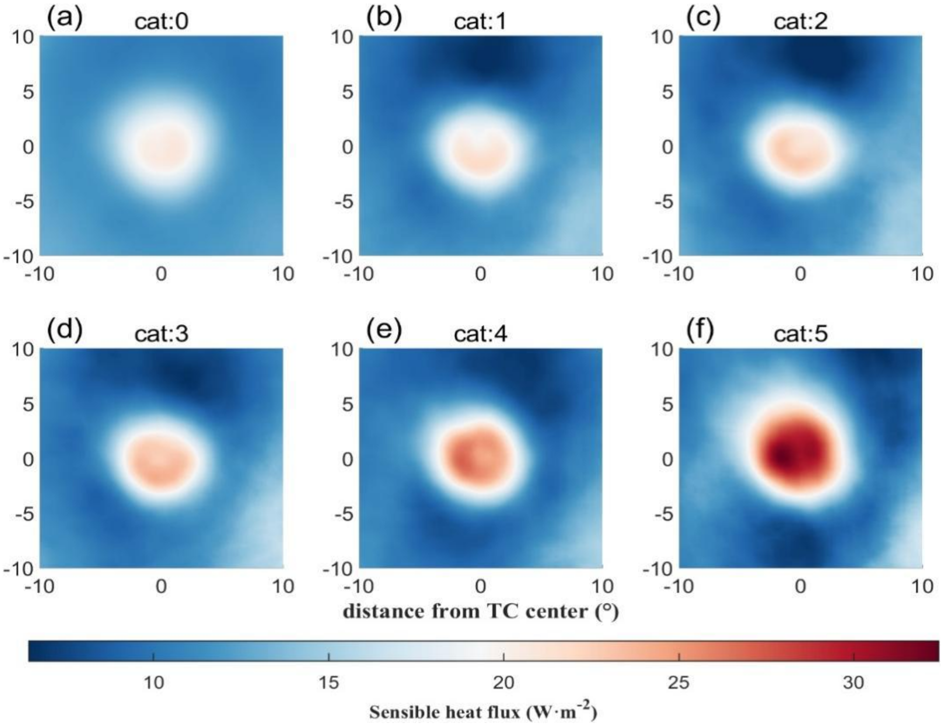

Figure S10: Plan views of composite surface sensible heat flux (W m^{-2}) centered on TC classified by TC intensity with (a) Cat 0, (b) Cat 1, (c) Cat 2, (d) Cat 3, (e) Cat 4, and (f) Cat 5 for ifremerflux.

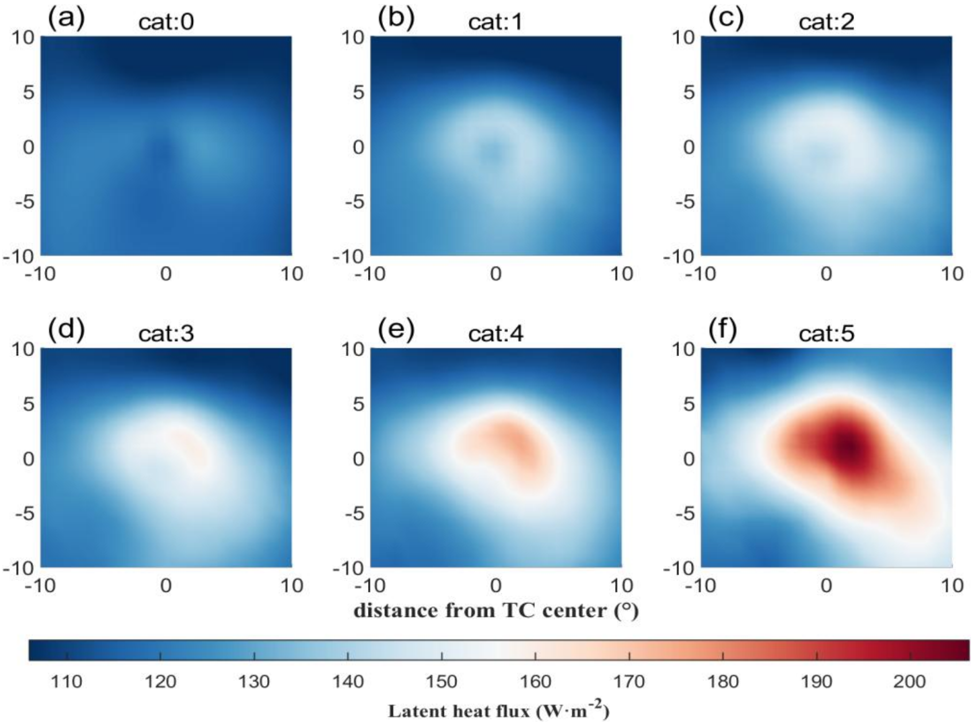

Figure S11: Plan views of composite surface latent heat flux (W m^{-2}) centered on TC classified by TC intensity with (a) Cat 0, (b) Cat 1, (c) Cat 2, (d) Cat 3, (e) Cat 4, and (f) Cat 5 for OAFlux.

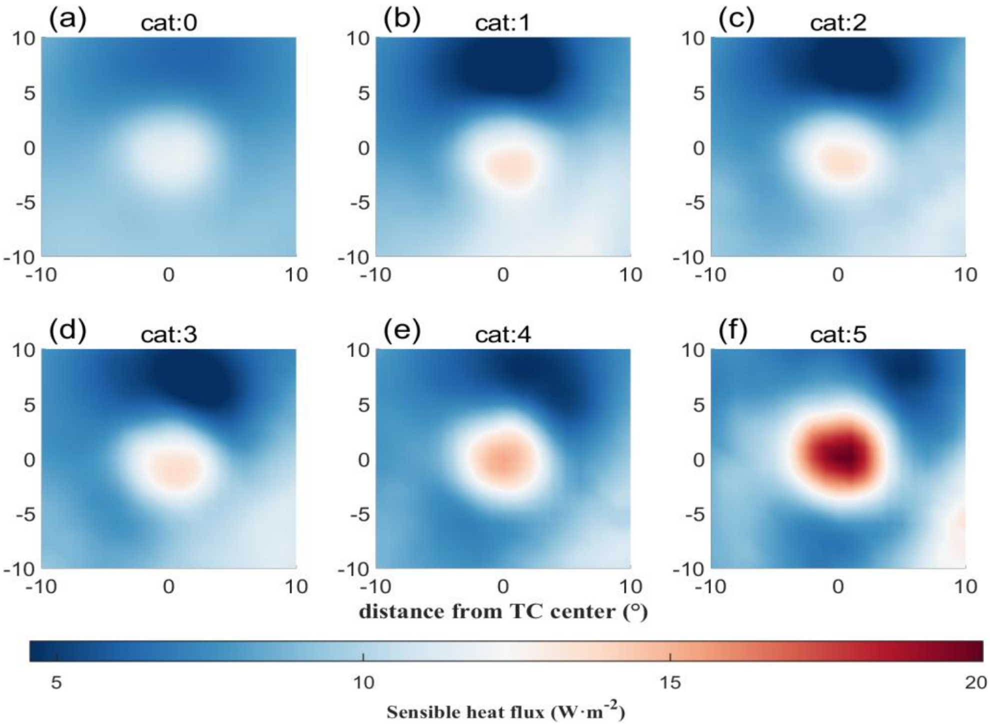

Figure S12: Plan views of composite surface sensible heat flux (W m^{-2}) centered on TC classified by TC intensity with (a) Cat 0, (b) Cat 1, (c) Cat 2, (d) Cat 3, (e) Cat 4, and (f) Cat 5 for OAFlux.

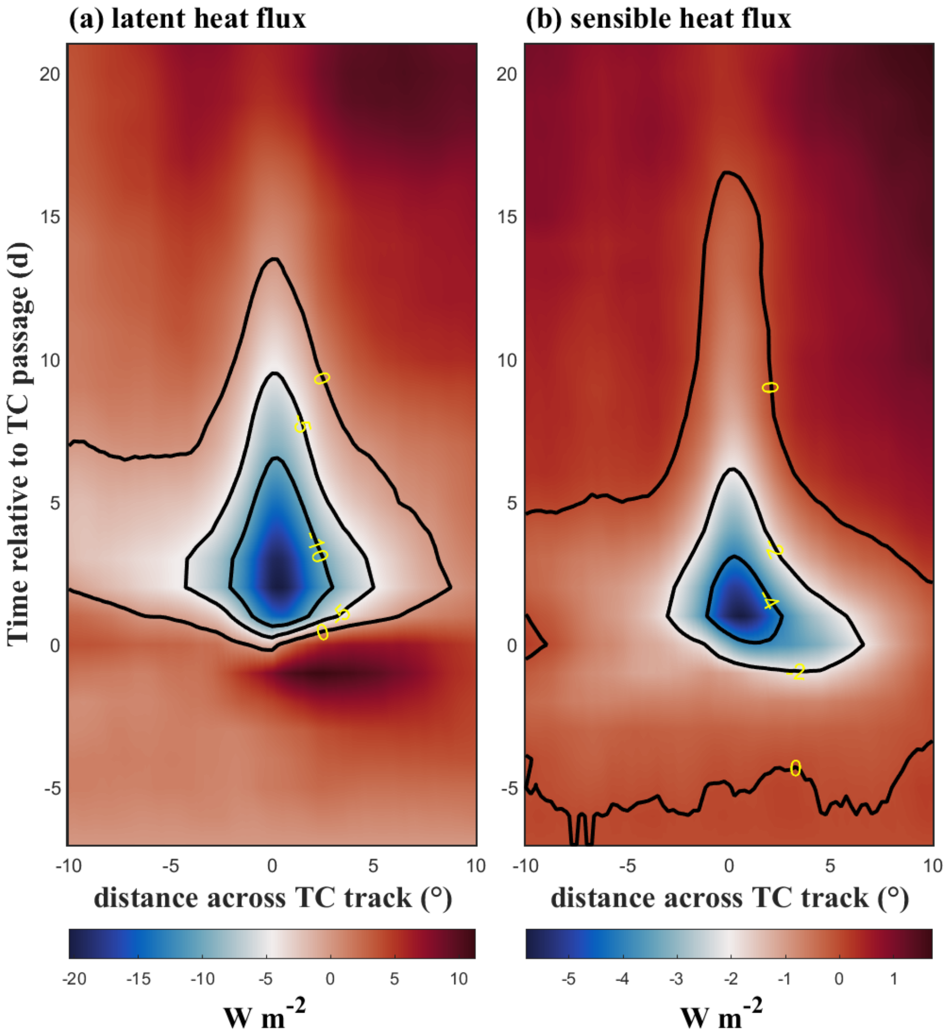

Figure S13: Temporal evolution of the along-track-averaged (±0.25°) composite (a) surface latent heat flux anomaly (W m^{-2}) and (b) surface sensible heat flux anomaly (W m^{-2}) across the TC track for J-OFURO 3.

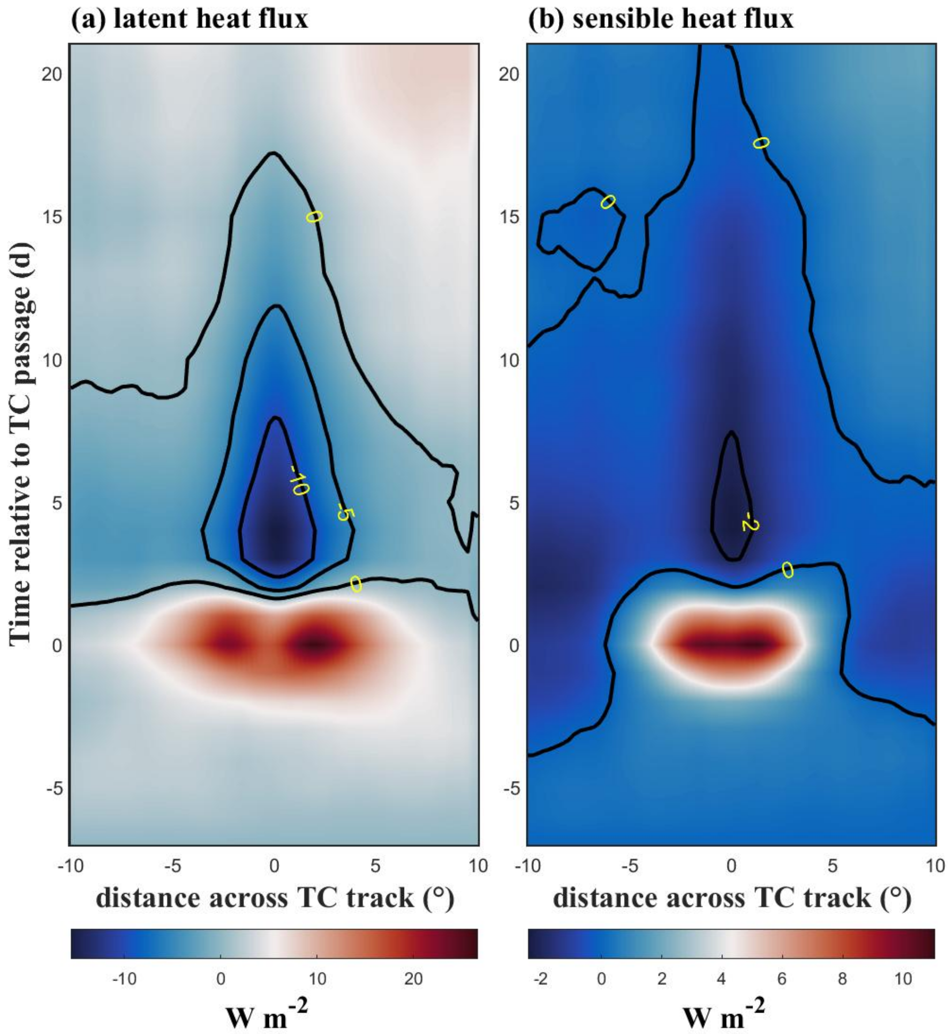

Figure S14: Temporal evolution of the along-track-averaged (±0.25°) composite (a) surface latent heat flux anomaly (W m^{-2}) and (b) surface sensible heat flux anomaly (W m^{-2}) across the TC track for ifremerflux.

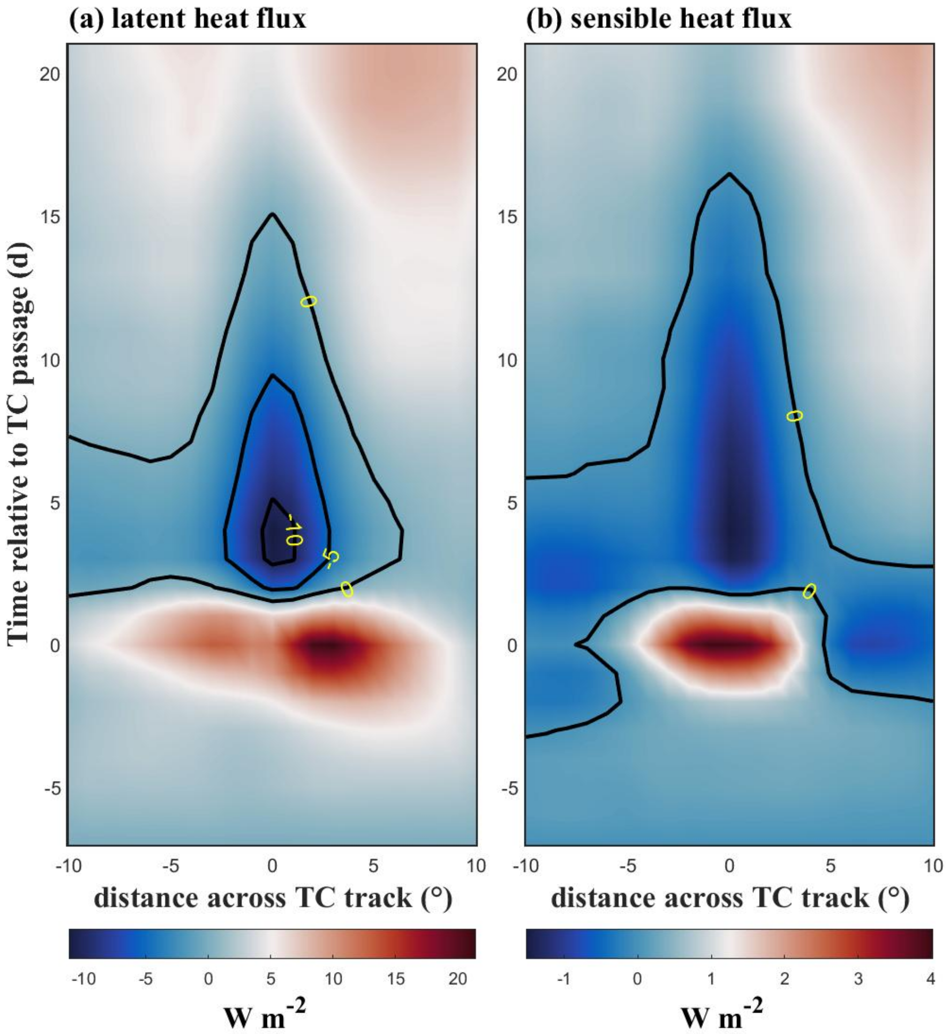

Figure S15: Temporal evolution of the along-track-averaged (±0.25°) composite (a) surface latent heat flux anomaly (W m^{-2}) and (b) surface sensible heat flux anomaly (W m^{-2}) across the TC track for OAFlux.

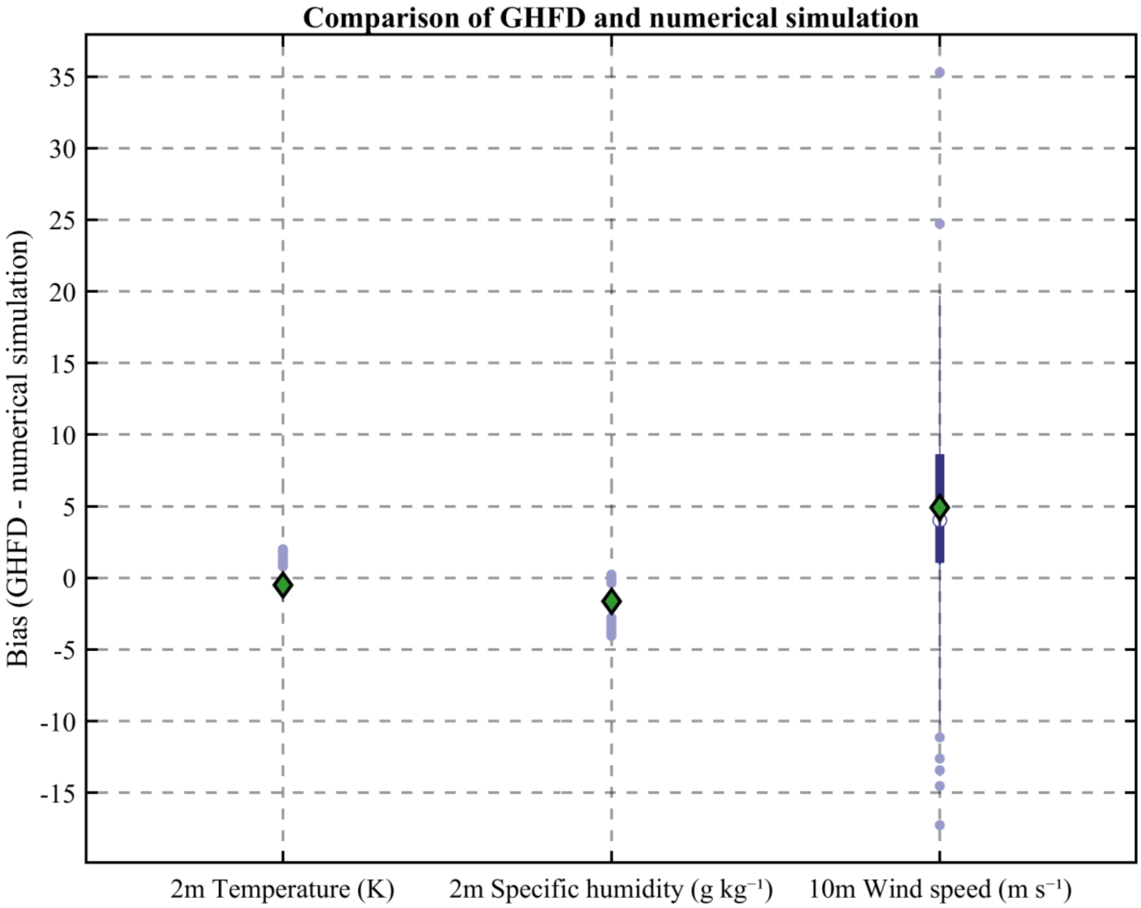

Figure S16: Box plots of bias between GHFD observations and numerical simulations for 2 m temperature (K), 2 m specific humidity (g kg^{-1}), and 10-m wind speed (m s^{-1}). Green diamonds denote the mean bias for each variable.